IOP Publishing Physics in Medicine and Biology

Phys. Med. Biol. **52** (2007) 6663–6678 doi:10.1088/0031-9155/52/22/008

Bayesian multiresolution method for local tomography in dental x-ray imaging

K Niinimäki[1], **S Siltanen**[2] **and V Kolehmainen**[1]

[1] Department of Physics, University of Kuopio, PO Box 1627, FIN-70211 Kuopio, Finland
[2] Institute of Mathematics, Tampere University of Technology, PO Box 553, FIN-33101 Tampere, Finland

E-mail: Kati.Niinimaki@uku.fi

Received 13 April 2007, in final form 7 June 2007
Published 26 October 2007
Online at stacks.iop.org/PMB/52/6663

Abstract

Dental tomographic cone-beam x-ray imaging devices record truncated projections and reconstruct a region of interest (ROI) inside the head. Image reconstruction from the resulting local tomography data is an ill-posed inverse problem. A new Bayesian multiresolution method is proposed for local tomography reconstruction. The inverse problem is formulated in a well-posed statistical form where a prior model of the target tissues compensates for the incomplete x-ray projection data. Tissues are represented in a wavelet basis, and prior information is modeled in terms of a Besov norm penalty. The number of unknowns in the reconstruction problem is reduced by abandoning fine-scale wavelets outside the ROI. Compared to traditional voxel-based models, this multiresolution approach allows significant reduction of degrees of freedom without loss of accuracy inside the ROI, as shown by 2D examples using simulated and *in vitro* local tomography data.

1. Introduction

We propose a Bayesian multiresolution method for three-dimensional dental x-ray imaging. Dental structures are represented in a reduced wavelet basis with finer details available only inside the region of interest (ROI). This way the computational effort is greatly reduced while accuracy is retained in the ROI.

Several diagnostic and operative tasks in dentistry require precise three-dimensional (3D) information about dental structures, and often two-dimensional (2D) x-ray images are not sufficient. For example, dental implantology is based on accurate measurements for the optimal depth, size and angle of the screw hole. The hole should be deep enough for firm attachment of the implant while avoiding damage to the mandibular nerve or penetration to the maxillary sinus (Ekestubbe *et al* 1997, Ramesh *et al* 2002).

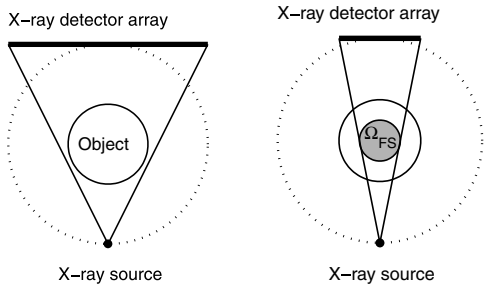

Figure 1. Global (left) and local (right) tomography. The source and detector panel rotate around the object along the dotted circle. Ω_{FS} represents the subdomain that is present in all of the projection images in the local tomography case. Usually the region of interest is chosen to be Ω_{FS}.

In recent years, tomographic devices dedicated to dental imaging have been introduced; see, for example, Soredex (2007), Planmeca Incorp. (2006), Imaging Sciences International (2006) and Hitachi Medical Corp. (2006). This imaging modality is called dental *cone beam computed tomography* (CBCT); typically a C-arm with an x-ray source and a digital detector rotates full circle around the patient's head and collects 2D projection data. CBCT imaging is an example of *local tomography*: the aim is to reconstruct a ROI from a set of *truncated* projection images (Smith and Keinert 1985, Faridani *et al* 1992, 1997, Maass 1992, Natterer 1986). See figure 1 for an illustration of the geometry. Compared to traditional CT scanners, the dental CBCT devices provide higher resolution, lower cost and a reduced radiation dose to the patient. However, CBCT produces *sparse projection data* as opposed to global and dense CT data, since the projections are truncated and possibly coarsely sampled in the angular variable. Image reconstruction from such data is an ill-posed inverse problem.

Bayesian inversion is a well-suited framework for the reconstruction from sparse projection data and it often outperforms traditional methods; the key idea is to formulate the inverse problem in a well-posed statistical form where a prior model of the tissues compensates for the limited information in the data. See Siltanen *et al* (2003) for a review and Hanson and Wecksung (1983), Sauer *et al* (1994), Bouman and Sauer (1993), Frese *et al* (2002) and Kolehmainen *et al* (2003) for examples of Bayesian methods for tomography.

The attenuation coefficient in x-ray tomography is often represented in piecewise constant voxel basis; see, e.g., Hanson and Wecksung (1983), Sauer *et al* (1994), Bouman and Sauer (1993) and Zheng *et al* (2000). Voxel-based total variation (TV) priors have been applied to dental x-ray imaging using sparse projection data in (Kolehmainen *et al* 2003, 2006). TV priors were introduced originally for modeling blocky objects (Rudin *et al* 1992, Dobson and Santosa 1994, 1996), and they have been found to perform well for dental structures which consist of a few different tissue types (soft tissue, bone, enamel) with crisp boundaries.

Voxel-based models are problematic for dental CBCT imaging because of the high resolution requirement. The dentist needs to see details of size $\sim$0.1 mm inside the ROI, but covering a volume Ω containing a cross-section of the head with voxels of size $0.1 \times 0.1 \times 0.1$ mm^3 leads to an impractically large number of unknowns in the inverse problem. One option could be to cover only the ROI with voxels and not to model other tissue at all. However, this typically leads to severe reconstruction artifacts.

We propose a Bayesian multiresolution method for dental x-ray imaging. We use a wavelet basis for the multiresolution representation of dental structures. The key idea is to use high resolution inside the ROI and coarser resolution elsewhere in the reconstruction volume Ω.

The intuition behind this multiresolution representation is the observation that the fine scale details of tissue structures outside the domain Ω_{FS} (see figure 1) cannot be reconstructed well (even in the qualitative sense) from local tomography data; see, e.g., Maass (1992) and Natterer (1986). By using the coarse representation outside the ROI, the contribution of the exterior tissues to the projection measurements can be taken satisfactorily into account, thus avoiding ghost artifacts that are due to the nonlocality of the projection measurements inside the ROI. Compared to voxel-based models, this multiresolution representation reduces the number of unknowns significantly without compromising reconstruction quality in the ROI. The reduction also leads to a less ill-posed reconstruction problem.

Our method uses a Besov space prior for the dental structures. The unknowns in the inverse problem are the wavelet coefficients, and the reconstruction is the *maximum a posteriori* (MAP) estimate for the coefficients. We test our method on 2D local tomography problems involving simulated CBCT data from phantoms and measured *in vitro* data from dental specimens. The 2D situation corresponds to CBCT reconstruction in the plane of rotation; we do not discuss the additional problems in 3D reconstruction from cone beam data. Λ-tomography and MAP estimates with TV-priors are given as references.

Let us review previous multiresolution approaches to tomography. In Steinberg and Heyman (1993), Olson and DeStefano (1994), Delaney and Bresler (1995), Bhatia *et al* (1996), Zhao *et al* (1997), Rashid-Farrokhi *et al* (1997), Madych (1999) and Bonnet *et al* (2000) filtered-backprojection-type methods with the help of the wavelet transform are used to recover the ROI in full angle local tomography. A set of sparse measurements far from the ROI is added to recover the low-resolution components of the image in Olson and DeStefano (1994) and Delaney and Bresler (1995). Sahiner and Yagle (1993) combine wavelets and filtered backprojection to recover an image from limited angle tomography data. In Zhong *et al* (2004) wavelets are used for denoising the projection images in CBCT imaging of breast tissues. Bayesian inversion methods with wavelet-based priors have been proposed in Frese *et al* (2002) and Rantala *et al* (2006), the former using a wavelet graph prior model and coarse-to-fine strategy for full angle global tomography data and the latter using a Besov space prior and a prethresholding procedure for limited angle tomography.

We note that an alternative basis for a similar multiresolution representation could be constructed using a family of rotationally symmetric interpolation functions with scalable width. One such example would be Gaussian interpolation functions. For further details on different interpolation functions in tomography, see Hanson and Wecksung (1985), Mueller (1998) and Lewitt (1992).

2. Wavelets and Besov spaces

Our discussion follows standard references such as Daubechies (1992), Meyer (1992), Keinert (2004) and Vidakovic (1999).

Let ϕ and ψ denote some compactly supported scaling and wavelet functions in a one-dimensional orthonormal multiresolution analysis (MRA). Then sufficiently regular functions $f : [0, 1] \to \mathbb{R}$ can be expanded as follows:

$$f(x) = \sum_{k=K_0(J_0)}^{K_1(J_0)} \langle f, \phi_{J_0 k}\rangle \phi_{J_0 k} + \sum_{j=J_0}^{\infty} \sum_{k=K_0(j)}^{K_1(j)} \langle f, \psi_{jk}\rangle \psi_{jk}, \tag{1}$$

where $\phi_{jk}(x) = 2^{\frac{j}{2}}\phi(2^j x - k)$ and $\psi_{jk}(x) = 2^{\frac{j}{2}}\psi(2^j x - k)$. The index j describes the scale of details and k represents translations; basis functions with fixed j represent details of f at a fixed scale. The scale-dependent upper and lower limits $K_0(j)$ and $K_1(j)$ are dictated by the

size of the supports of ϕ and ψ: we take care of boundary effects by including in expansion (1) only those basis functions whose support intersects the interval [0, 1].

Suppose our starting point is a finite collection of function values $f(x_v)$ on a regular grid $x_1, \ldots, x_m$. With a suitable choice of ϕ and ψ the coefficients $\langle f, \phi_{J_0 k}\rangle$ and $\langle f, \psi_{jk}\rangle$ can be computed very efficiently as convolutions with finite impulse responses. Note that the sum over j in (1) is then taken up to $J-1$ with some $J > J_0$ determined by the number m of sample points. One possible choice of ϕ and ψ with the above properties is to take them from the Daubechies family.

There are several ways of constructing MRA and wavelets in two dimensions. We use the standard tensor product construction with the scaling and wavelet functions

$$\begin{aligned} &\phi(x) = \phi(x_1)\phi(x_2), \\ &\psi^1(x) = \phi(x_1)\psi(x_2), \quad \psi^2(x) = \psi(x_1)\phi(x_2), \quad \psi^3(x) = \psi(x_1)\psi(x_2). \end{aligned} \tag{2}$$

Similarly to the one-dimensional case, let us denote

$$\phi_{jk}(x) = 2^j \phi(2^j x - z_{jk}), \qquad \psi_{jk\ell}(x) = 2^j \psi^\ell(2^j x - z_{jk}), \tag{3}$$

where index $j \in \mathbb{Z}$ refers to the scale and ℓ to the wavelet type, with $\ell = 1$ being the horizontal details wavelet, $\ell = 2$ vertical details and $\ell = 3$ diagonal details. The index k refers to the spatial location z_{jk} of the form $(\nu_1 2^{-j}, \nu_2 2^{-j})$ with $\nu_1, \nu_2 \in \mathbb{Z}$. We include only basis functions whose support intersects $[0, 1]^2$ and number the spatial locations with just one index k.

Assume given a function $f : [0, 1]^2 \to \mathbb{R}$ in the form of a discrete image with m pixels. Similarly to the 1D case, f can now be expanded as

$$f = \sum_{k=K_0(J_0)}^{K_1(J_0)} c_{J_0 k}\phi_{J_0 k} + \sum_{j=J_0}^{J-1} \sum_{k=K_0(j)}^{K_1(j)} \sum_{\ell=1}^{3} w_{jk\ell}\psi_{jk\ell}, \tag{4}$$

where $c_{J_0 k} := \langle f, \phi_{J_0 k}\rangle$ and $w_{jk\ell} := \langle f, \psi_{jk\ell}\rangle$. Again, the coefficients $c_{J_0 k}$ and $w_{jk\ell}$ allow fast computation when Daubechies wavelets are used. We write (4) in matrix form as

$$f = Bw = B \begin{bmatrix} (c_{J_0 k}) \\ (w_{jk\ell}) \end{bmatrix} \in \mathbb{R}^{n_f}, \tag{5}$$

where B is the $m \times n_f$ matrix implementing (4).

Besov function spaces $B^s_{pq}(\mathbb{R}^2)$ with parameters $1 \leqslant p, q \leqslant \infty$ and smoothness index $s \in \mathbb{R}$ can be used to model piecewise smooth targets such as dental tissue. If the chosen wavelet system is sufficiently smooth, a Besov space norm can be written in terms of the wavelet coefficients (Daubechies 1992, Meyer 1992, Härdle *et al* 1998, Jaffard 2004, Choi and Baraniuk 2004, Chambolle *et al* 1998):

$$\|f\|_{B^s_{pq}} = \left(\sum_{k=K_0(J_0)}^{K_1(J_0)} |c_{j_0 k}|^p \right)^{\frac{1}{p}} + \left[\sum_{j=J_0}^{\infty} \left(2^{j(s+\frac{1}{2}-\frac{1}{p})} \left(\sum_{k=K_0(j)}^{K_1(j)} \sum_{\ell=1}^{3} |w_{jk\ell}|^p \right)^{\frac{1}{p}} \right)^q \right]^{\frac{1}{q}}.$$

In this work we take $p = q$ and use the computationally effective norm $\|f\|_{ps}$ defined by

$$\|f\|_{ps}^p := \sum_{k=K_0(J_0)}^{K_1(J_0)} |c_{j_0 k}|^p + \sum_{j=J_0}^{J-1} \sum_{k=K_0(j)}^{K_1(j)} \sum_{\ell=1}^{3} 2^{jp(s+\frac{1}{2}-\frac{1}{p})} |w_{jk\ell}|^p. \tag{6}$$

3. Bayesian inversion with wavelets and Besov norm prior

3.1. Bayesian inversion

As general references to Bayesian inversion, see Hanson (1987), Lehtinen (1988), Mosegaard and Tarantola (1995), Nicholls and Fox (1998) and Kaipio and Somersalo (2005).

In the Bayesian inversion approach the inverse problem is considered as a problem of statistical inference. All the unknown variables are modeled as random variables. The statistical modeling of these variables reflects our uncertainty of their actual values and the degree of uncertainty is coded in their probability distributions.

Let y denote the measured data and f the unknown parameters to be determined. Bayes' theorem yields the posterior distribution

$$\pi_{\text{post}}(f) = \pi(f|y) = \frac{\pi(y|f)\pi_{\text{pr}}(f)}{\pi(y)} \tag{7}$$

that represents the complete solution of the inverse problem. In equation (7) $\pi(y|f)$ is the *likelihood function*, $\pi_{\text{pr}}(f)$ is the *prior density* and $\pi(y)$ is a normalization constant.

The likelihood function is a statistical model for the observations; it describes the probability that the measured data y are observed from a given realization f. The prior density $\pi_{\text{pr}}(f)$ is a statistical model for the unknown f based on *a priori* information.

The solution $\pi_{\text{post}}(f)$ can be summarized and visualized by various statistics. The most common choice for the estimate that is displayed as the reconstructed image is the *maximum a posteriori* (MAP) estimate

$$f_{\text{MAP}} = \arg\max_f \pi_{\text{post}}(f). \tag{8}$$

3.2. Bayesian model for x-ray tomography with wavelets and Besov norm prior

The x-ray projection images of the target can be considered as line integrals of the tissue attenuation density along the lines between the source and detector points. Within the discrete framework these observations are represented by the model

$$y = Af + \epsilon, \qquad \epsilon \sim \mathcal{N}(0, \Gamma_\epsilon), \tag{9}$$

where $y \in \mathbb{R}^q$ is the vector of measured projection data (all the projections concatenated into a single vector), $f \in \mathbb{R}^m$ is a vector that represents the attenuation function (pixel values) at given locations in the image domain Ω and A is a matrix that implements the transformation from the pixel values to the projection data. The discretization is assumed to be such that the whole object is embedded inside the image domain Ω. Vector $\epsilon \in \mathbb{R}^q$ represents the measurement noise, which is assumed zero mean Gaussian with covariance matrix Γ_ϵ. The validity of this noise model (9) is discussed in Bouman and Sauer (1993) and Siltanen *et al* (2003).

In model (9) we neglect scattering phenomena and effects of non-monochromatic radiation such as beam hardening. See Sauer *et al* (1994) and Antyufeev and Bondarenko (1996) for the former, and Sudovic and Clonthorne (2000) for the latter.

With the above model, the likelihood function becomes

$$\pi(y|f) = C_1 \exp\left(-\tfrac{1}{2}\|L_\epsilon(Af - y)\|_2^2\right), \tag{10}$$

where $L_\epsilon^{\mathrm{T}} L_\epsilon = \Gamma_\epsilon^{-1}$ and C_1 is a normalizing constant. Using (5), the observation model (9) can be written as $y = ABw + \epsilon$, leading to the likelihood model

$$\pi(y|w) = C_1 \exp\left(-\tfrac{1}{2}\|L_\epsilon(ABw - y)\|_2^2\right). \tag{11}$$

As the prior model for the unknown image f we use a density that prefers a small Besov norm. Using equations (6) and (5) the prior model can be written as

$$\pi_{\mathrm{pr}}(w) = C_2 \exp\left(-\alpha \|Bw\|_{ps}^p\right). \tag{12}$$

The posterior distribution for the wavelet coefficients of the unknown f is now

$$\pi_{\mathrm{post}}(w) = C \exp\left(-\tfrac{1}{2}\|L_\epsilon(ABw - y)\|_2^2 - \alpha \|Bw\|_{ps}^p\right). \tag{13}$$

3.3. Computation of the MAP estimate

To obtain a single representative of the solution, we compute the MAP estimate

$$w_{\mathrm{MAP}} = \arg\max_w \pi_{\mathrm{post}}(w), \tag{14}$$

and display the image Bw_{MAP} as the tomographic reconstruction of the target. The maximizer w_{MAP} can be obtained by minimizing the functional in the exponent:

$$w_{\mathrm{MAP}} = \arg\min_w F(w) := \arg\min_w \left\{\tfrac{1}{2}\|L_\epsilon(ABw - y)\|_2^2 + \alpha \|Bw\|_{ps}^p\right\}. \tag{15}$$

If $p > 1$ then $F(w)$ is differentiable, strictly convex, and has a unique minimum.

The minimization is realized using the nonlinear conjugate gradient Polak–Ribière optimization method, which can be written as

$$w_{(i+1)} = w_{(i)} + s_{(i)} d_{(i)}, \tag{16}$$

where $s_{(i)}$ is the step parameter, $d_{(i)}$ is the search direction and i is the iteration index. The search direction is calculated at each step by

$$d_{(i+1)} = -g_{(i+1)} + \beta_{(i)} d_{(i)}, \tag{17}$$

where $g_{(i)}$ is the gradient of $F(w)$ at $w_{(i)}$ and

$$\beta_{(i)} = \frac{g_{(i+1)}^T (g_{(i+1)} - g_{(i)})}{\|g_{(i)}\|^2}. \tag{18}$$

The initial search direction is $d_{(0)} = -g_{(0)}$ (Dai and Yuang 1999). The step parameter $s_{(i)}$ is found by an explicit line search algorithm.

4. Multiresolution model for local tomography using wavelets

The key idea in the multiresolution model is to reduce the number of unknowns in the local tomography problem using high resolution only in the region of interest Ω_{ROI} and lower resolution elsewhere in the image domain. The wavelet representation (5) is well suited for this because of its locality and scaling properties (Daubechies 1992, Aboufadel and Schlicker 1999): all the wavelet coefficients up to the finest available scale J are used inside the ROI (i.e., $J_{\mathrm{roi}} = J$) and only a partial number ($J_{\mathrm{out}} < J$) of the scaling levels are used elsewhere in the image domain.

Let $\mathcal{I} = \{1, 2, \ldots, n_f\}$ denote the indexing of the basis in the wavelet expansion $w \in \mathbb{R}^{n_f}$ when all the J scales are used everywhere in the image domain Ω (see equation (5)). Now, by denoting by $\mathcal{S} \subset \mathcal{I}$ the set of basis indices that contain (i) all the scales up to J in Ω_{ROI} and (ii) the scales up to J_{out} in $\Omega \backslash \Omega_{\mathrm{ROI}}$, we can (formally) write

$$f = \tilde{B}\tilde{w}, \qquad \tilde{w} = Pw \in \mathbb{R}^n, \qquad \tilde{B} = BP^T, \qquad n \leqslant n_f \tag{19}$$

for the desired multiresolution representation of the image f. In equation (19) P is a $n \times n_f$ model reduction matrix with elements of the form

$$P_{i,j} = \begin{cases} 1, & \mathcal{S}_i = j \\ 0, & \text{otherwise,} \end{cases}$$

where $\mathcal{S}_i$ denotes the ith element of set $\mathcal{S}$.

Using equation (19), we write the reduced model $y = A\tilde{B}\tilde{w} + \epsilon$ for the projection measurements in the multiresolution approach. Using this model and following section 3.2, we obtain the posterior model

$$\pi_{\text{post}}(\tilde{w}) = \tilde{C} \exp\left(-\tfrac{1}{2}\|L_\epsilon(A\tilde{B}\tilde{w} - y)\|_2^2 - \alpha\|\tilde{B}\tilde{w}\|_{ps}^p\right) \tag{20}$$

for the multiresolution problem. The computation of the MAP estimate in this framework results in solving the minimization problem

$$\tilde{w}_{\text{MAP}} = \arg\min_{\tilde{w}} F(\tilde{w}) := \arg\min_{\tilde{w}} \left\{\tfrac{1}{2}\|L_\epsilon(A\tilde{B}\tilde{w} - y)\|_2^2 + \alpha\|\tilde{B}\tilde{w}\|_{ps}^p\right\}, \tag{21}$$

where the functional $F(\tilde{w})$ is differentiable and strictly convex for $p > 1$.

5. Materials and methods

The performance of the multiresolution method is evaluated with 2D examples using simulated and *in vitro* data. Two different test cases are considered:

(i) *Simulated local tomography data from a jawbone phantom.* The data consist of 187 projections from a total opening angle of 187° (projection interval 1°). This is an example of dental CBCT imaging.

(ii) *Experimental local tomography data from a jawbone specimen.* The projection data were collected from sparsely distributed directions (23 projections from a total opening angle of 187°, projection interval 8.5°). This is an example of dental CBCT with a small number of projections.

We use the maximum available number J of scaling levels inside Ω_{ROI} and study the effect of decreasing the number J_{out} of scaling levels outside the ROI. We measure this effect quantitatively using the following relative errors,

$$\delta_G(f) = \frac{\|f_{\text{true}} - f\|_{L^2(G)}}{\|f_{\text{true}}\|_{L^2(G)}} \times 100\%, \tag{22}$$

either in the whole image domain ($G = \Omega$) or in the ROI ($G = \Omega_{\text{ROI}}$).

As a reference method for the multiresolution reconstruction we use the pixel-based MAP estimate with the total variation prior. TV prior is known to produce good reconstructions in dental applications (Kolehmainen *et al* 2003, 2006). For examples of TV priors in other applications of x-ray tomography and imaging problems, see Dobson and Vogel (1997), Vassilevski and Wade (1997), Delaney and Bresler (1998), Kaipio *et al* (2000), Persson *et al* (2001), Candes *et al* (2005) and Sidky *et al* (2006).

The (approximate) total variation (TV) for the pixel image f can be written as

$$\text{TV}_\beta(f) = \sum_{i=1}^{m} \sum_{j \in \mathcal{N}_i} \sqrt{(\beta + (f_i - f_j)^2)}, \tag{23}$$

where $\mathcal{N}_i$ denotes the usual four-point neighborhood for the pixel i and β is a smoothing parameter. The total variation prior can be written as

$$\pi_{\text{pr}}(f) \propto \exp(-\lambda \text{TV}_\beta(f)). \tag{24}$$

When the noise model (9) is used, the computation of the MAP estimate with the TV prior amounts to minimizing

$$F_{\mathrm{TV}}(f) = \tfrac{1}{2}\|L_\epsilon(Af - y)\|_2^2 + \lambda \mathrm{TV}_\beta(f). \tag{25}$$

The key idea in the multiresolution method is reducing the number of unknowns by using accurate resolution only inside Ω_{ROI}. In the pixel domain, a brute force way for analogous reduction is to use Ω_{ROI} as the whole image domain in the model and neglect the contribution of the tissues outside the ROI to the projection measurements. Let $\mathcal{J}$ denote the index set of pixels inside the Ω_{ROI} in the measurement model (9). Then the measurement model for the ROI-only model ($\Omega = \Omega_{\mathrm{ROI}}$) can be obtained as

$$y \approx A_{\mathrm{ROI}} f_{\mathrm{ROI}} + \epsilon, \qquad A_{\mathrm{ROI}} := A(:, \mathcal{J}), \qquad f_{\mathrm{ROI}} := f(\mathcal{J}). \tag{26}$$

The total variation reconstructions using model (26) are also given as reference reconstructions for the proposed multiresolution method in both examples.

In test case (ii) we also compare our new method to the Λ-tomography reconstruction in Kolehmainen *et al* (2003) using the same *in vitro* local tomography data. Λ-tomography is a reconstruction method that has been specifically designed for local tomography; see Smith and Keinert (1985) and Faridani *et al* (1992, 1997).

All computations are done with a desktop PC (model: Intel® Pentium® 4 CPU 3.2 GHz with 4 GB RAM) using Matlab® version 7.2 (R2006a).

6. Results and discussion

We use the following choices in all computations. Daubechies 6 wavelets are used in the multiresolution model (20). The parameters (p, q, s) are chosen as $p = 1.5, q = 1.5$ and $s = 0.5$. These values are well suited for dental imaging (Rantala *et al* 2006). The value $\alpha = 30$ is used for the width parameter of the Besov prior in all the reconstructions. The parameters of the TV prior are $\lambda = 0.1$ and $\beta = 10^{-4}$. The parameters in both models, the TV prior and the Besov prior, were tuned to give the best visual image quality.

6.1. Simulated local tomography data from a jawbone phantom

The jawbone phantom that was used for the simulation of the projection data is shown on the left in figure 2. The simulated phantom was constructed by imaging a dry skull phantom with a hospital CT scanner. The simulated phantom is one 2D slice from the 3D reconstruction.

The size of the phantom was 300×300 pixels. The local tomography data were simulated using a small detector panel, leading to a projection geometry where the subdomain Ω_{FS}, i.e., the subdomain that is visible in all projections encloses the three teeth on the right-hand side of the jawbone. The region of interest in the local tomography problem was chosen to be $\Omega_{\mathrm{ROI}} = \Omega_{\mathrm{FS}}$ (the ROI is denoted by the white circle). The number of line integrals in each of the 187 projections was chosen to be 300, leading to the projection data vector $y \in \mathbb{R}^{56100}$. Additive Gaussian noise $\epsilon \sim \mathcal{N}(0, \sigma^2)$ with a standard deviation of 1% of the maximum of the computed projections was added to the simulated data.

In the inverse problem, the size of the pixel grid over the whole image domain Ω was chosen to be 256×256, leading to the number of unknowns $m = 65\,536$ in the pixel domain reconstructions.

Figure 2 shows reconstructions of the jawbone phantom with the multiresolution model from the simulated local tomography data. The image on the second column in figure 2 shows the MAP estimate when all $J = 5$ scaling levels were used inside the ROI but only the $J_{\mathrm{out}} = 1$

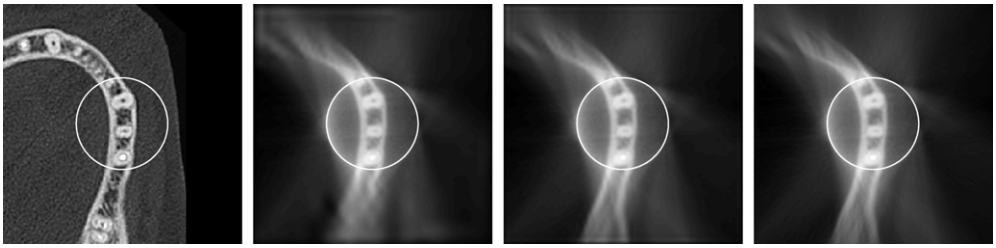

Figure 2. MAP estimates with the multiresolution model from the local tomography data of the jawbone phantom (in the first column). The ROI is marked with a white circle. In all the reconstructions, the number of scaling levels inside the ROI was $J = 5$. The number of the scaling levels outside the ROI was from the second to the fourth column $J_{\text{out}} = 1$, $J_{\text{out}} = 3$ and $J_{\text{out}} = 5$, respectively.

Table 1. The effect of the number (J_{out}) of scaling levels outside the ROI on the relative L^2-reconstruction error (22) in the local tomography reconstructions with the multiresolution model. The number of scaling levels inside the ROI was $J = 5$ in all cases. n is the number of unknown wavelet coefficients in the inverse problem. δ_G^W indicates the reconstruction error when the full wavelet basis reconstruction with $J_{\text{out}} = 5$ is used as the reference.

J_{out}	1	2	3	4	5
n	14 070	15 120	18 800	31 470	76 990
δ_Ω (%)	36.6	36.6	36.4	36.4	36.3
δ_{Ω^W} (%)	4.1	3.9	2.8	1.6	0
$\delta_{\Omega_{\text{ROI}}}$ (%)	24.0	23.9	23.8	23.7	23.7
$\delta_{\Omega^W_{\text{ROI}}}$ (%)	0.35	0.28	0.14	0.04	0

scaling level was used elsewhere in the image domain Ω. In the third and fourth columns, the numbers of scaling levels outside the ROI were $J_{\text{out}} = 3$ and $J_{\text{out}} = 5$, respectively. Table 1 shows the relative errors (22) in the whole image domain ($G = \Omega$) and in the ROI ($G = \Omega_{\text{ROI}}$) with respect to the varying number of scaling levels outside the ROI. The relative errors (22) are computed with respect to both the original phantom and the full wavelet basis reconstruction that uses all the $J_{\text{out}} = 5$ scaling levels outside the ROI. The computation times for the MAP estimates were 3 min 18 s for the full wavelet reconstruction ($J_{\text{out}} = 5$) and 1 min 40 s for the reconstruction using only the coarsest ($J_{\text{out}} = 1$) scaling level outside the ROI.

The reconstruction with the reference method is presented in figure 3. The image in the middle shows the MAP estimate with the TV prior ($m = 65\,536$, the relative error $\delta_{\Omega_{\text{ROI}}} = 23.7\%$, computation time 2 min 55 s). The right image shows the MAP estimate with the multiresolution model when only the coarsest scaling level ($J_{\text{out}} = 1$) was used outside the ROI (the number of unknown wavelet coefficients $n = 14\,070$, $\delta_{\Omega_{\text{ROI}}} = 24.0\%$, computation time 1 min 40 s). The ROI details from the images in figure 3 are displayed in figure 4.

The left image in figure 5 shows reconstruction with the TV prior when the partial measurement model (26) is used (i.e, the whole image domain is modeled as $\Omega = \Omega_{\text{ROI}}$). The number of unknown pixels in this case was $m = 7484$ and the reconstruction error $\delta_{\Omega_{\text{ROI}}} = 123.7\%$. Note that the image has high amplitude errors near the boundary. These errors are due to neglecting the contribution of the tissues outside the ROI to the measured projections; loosely speaking, the estimation algorithm tries to compensate this discrepancy between the model and measurements by introducing spurious details near the boundary

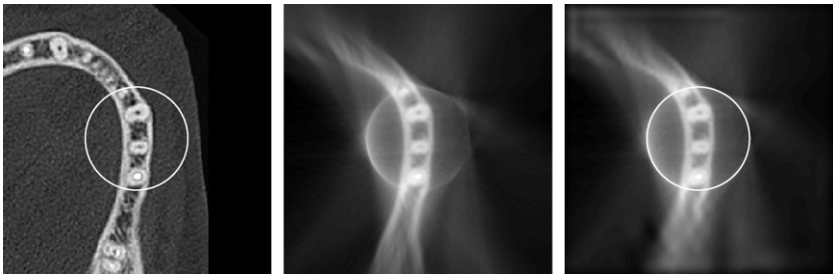

Figure 3. Reconstructions of the jawbone phantom from local tomography data. Columns from left to right: the phantom, the MAP estimate with the total variation prior, the MAP estimate with the multiresolution model using $J_{\text{out}} = 1$ scaling levels outside the ROI while the number of scaling levels inside the ROI was $J = 5$ (right). The ROI (Ω_{ROI}) is denoted by the white circle.

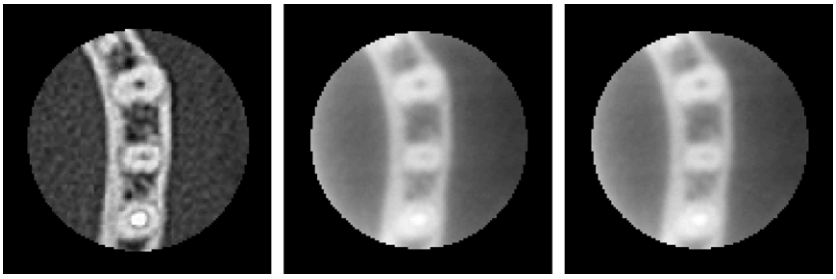

Figure 4. The ROI from the local tomography reconstructions in figure 3. Columns from left to right; the phantom, the MAP estimate with the total variation prior, the MAP estimate with the multiresolution model using $J_{\text{out}} = 1$ scaling levels outside the ROI while the number of scaling levels inside the ROI was $J = 5$.

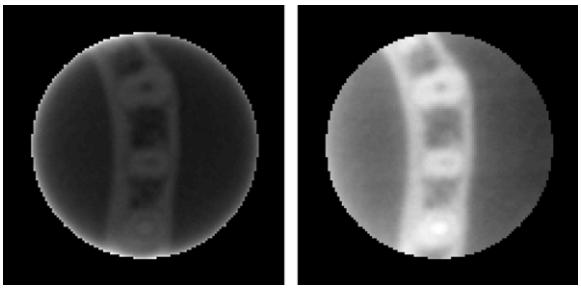

Figure 5. Local tomography of the jawbone phantom. Left: MAP estimate with the total variation prior when the matrix A_{ROI} is used as the forward model (i.e., the whole image domain $\Omega = \Omega_{\text{ROI}}$). Right: MAP estimate with the multiresolution model using $J_{\text{out}} = 1$ scaling levels outside the ROI while the number of scaling levels inside the ROI was $J = 5$. (Note that each image has its own gray scale.)

$\partial\Omega_{\text{ROI}}$. The right image shows the reconstruction from the right in figure 4, that is, the MAP estimate with the multiresolution model using all the $J = 5$ scaling levels inside the ROI and only the coarsest level $J_{\text{out}} = 1$ elsewhere in the image domain Ω (the number of unknown wavelet coefficients $n = 14070$, $\delta_{\Omega_{\text{ROI}}} = 24.0\%$).

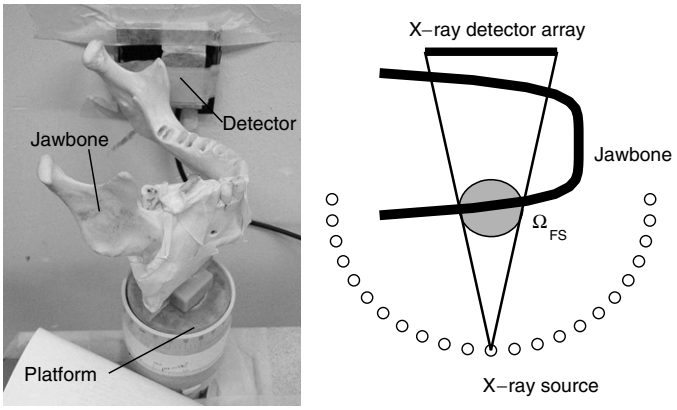

Figure 6. Left: a photograph of the measurement setup. Right: an illustration of the measurement geometry for the experiment with the jaw bone specimen.

The results in figures 2–5 and table 1 show that the proposed multiresolution model performs well in local tomography. From figure 2 and table 1 it can be seen that the ROI is reconstructed with very similar accuracy despite the number of scaling levels used outside the ROI. Also, another apparent feature is that the reconstruction quality outside the ROI remains similar with the different number of scaling levels used; this can be viewed as indirect evidence that the multiresolution model reduces successfully the redundancy from the local tomography problem. Further, figures 3–4 and the computed error estimates show that the reconstruction of the ROI domain with the multiresolution model is very similar to the reconstruction with the TV priors despite using only the coarsest level of scaling outside the ROI. Also, to reduce the number of unknowns to a level comparable to the multiresolution model in the pixel domain, the MAP estimate with the TV prior using the partial measurement model A_{ROI} (i.e., the truncated computation domain $\Omega = \Omega_{\mathrm{ROI}}$) was computed (see figure 5). The use of the truncated image domain resulted in an inferior reconstruction quality compared to the multiresolution model. These results suggest that the proposed multiresolution model offers tools for high quality reconstruction of the ROI in local tomography with a significantly smaller number of unknowns that are needed in the conventional pixel-based models.

6.2. Experimental local tomography data from a jawbone specimen

The projection radiographs of the jawbone specimen were acquired using a commercial intraoral x-ray detector (Sigma) and a dental x-ray source (Focus[3]). The Sigma detector is a 872 × 664-pixel CCD-detector with an imaging area of 34 mm × 26 mm. The projection images of the jawbone specimen were acquired using similar cone beam computed tomography geometry that is used in the commercial dental CBCT scanners. This experimental setup was constructed as follows: the x-ray source and the CCD-detector were placed into fixed positions such that the source direction was normal to the detector plane. The distance from the focal spot to the detector array was 138 cm. The jawbone specimen was placed on a rotating platform so that projections from different directions can be taken. The distance from the center of rotation to the detector was 8.8 cm. A photograph of the experimental setup is shown in the left image in figure 6. Using this setup, 23 projection images from a total view angle

[3] Sigma and Focus are registered trademarks of PaloDEx Group, Finland.

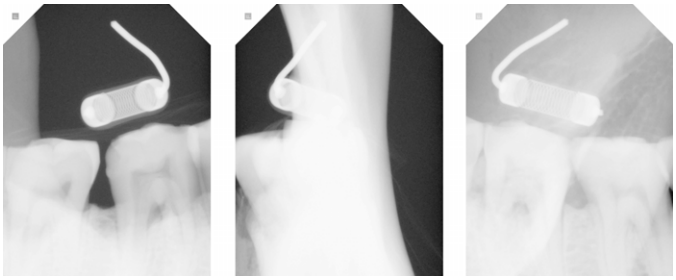

Figure 7. Projection images of the jawbone phantom. The locations of the legs of the electrical resistor that is seen in the projections were used for determining the accurate location of the center of rotation in the projection geometry. The three projections displayed are taken with approximately 90° intervals.

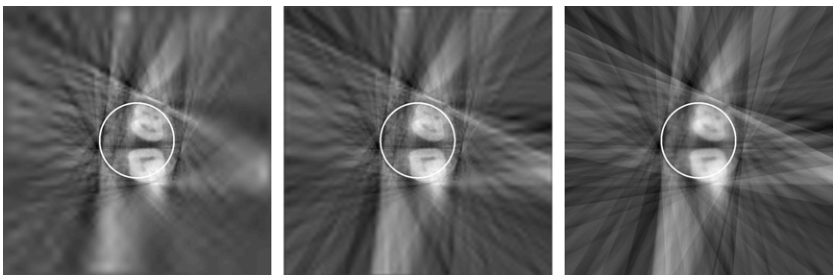

Figure 8. MAP estimates with the multiresolution model from the measured local tomography data of the jaw bone specimen. In all the reconstructions, the number of scaling levels inside the region of interest (ROI) was $J = 6$. The number of the scaling levels outside the ROI was from left to right $J_{\text{out}} = 1$, $J_{\text{out}} = 3$ and $J_{\text{out}} = 6$, respectively. The ROI is marked with a white circle.

of 187° were taken. The right image in figure 6 illustrates the projection geometry for the experiments. Figure 7 shows three of the projection images of the jawbone phantom.

One row from these projection images (matrices) was used for the 2D reconstruction. The number of data with this arrangement was $23 \times 664 = 15272$ (i.e., $y \in \mathbb{R}^{15\,272}$). In the computations, a square domain Ω with side length equivalent to three times the detector width ($3 \times 26 = 78$ mm) was chosen as the image domain Ω, which was then divided to 498×498 pixels. With this discretization, the number of unknowns in the pixel-based reconstruction becomes $m = 498 \times 498 = 248\,004$.

Figure 8 shows the reconstructions from the experimental projection data with the multiresolution model. The ROI is marked with the white circle in the images. In all the reconstructions, the number of scaling levels was $J = 6$ inside the ROI and the number J_{out} of the scaling levels outside the ROI was varied between $(1, 2, \ldots, 6)$. The left image in figure 8 shows the reconstruction using $J_{\text{out}} = 1$ scaling levels outside the ROI (the number of unknown wavelet coefficients $n = 29\,130$), the middle image shows reconstruction with $J_{\text{out}} = 3$ ($n = 34\,380$) and the right image shows reconstruction with $J_{\text{out}} = 6$($n = 269\,310$) The computation times were 14 min 54 s using the full wavelet model ($J_{\text{out}} = 6$) and 2 min 14 s using the multiresolution representation with only the coarsest scaling level ($J_{\text{out}} = 1$) outside the ROI.

Figure 9 shows the reconstructions with the reference methods. The top row shows the whole image domain Ω and the bottom row the ROI details. The result of the Λ-tomography

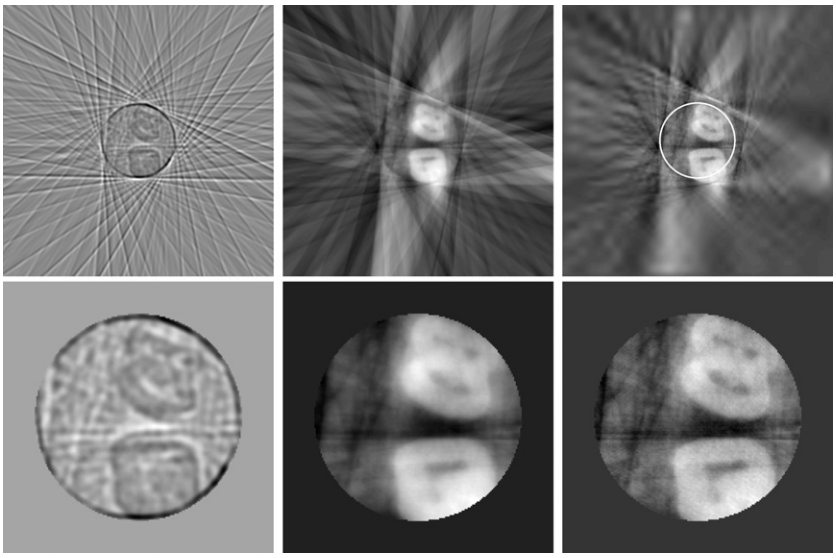

Figure 9. Reconstructions from the measured local tomography data of the jawbone specimen. Top row: the whole image domain Ω. Bottom row: the ROI detail. Columns from left to right: the Λ-tomography, the MAP estimate with the total variation prior, the MAP estimate with the multiresolution model using $J_{\text{out}} = 1$ scaling levels outside the ROI while the number of scaling levels inside the ROI was $J = 6$.

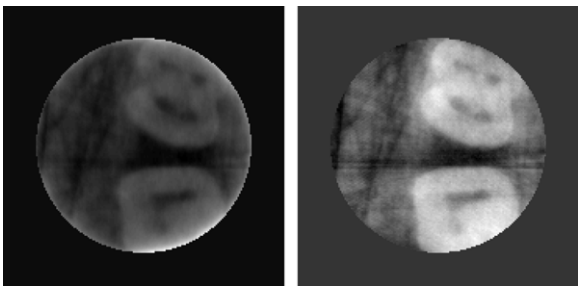

Figure 10. Reconstructions from the measured local tomography data of the jawbone specimen. Left: MAP estimate with the total variation prior when the matrix A_{ROI} is used as the forward model (i.e., the whole image domain $\Omega = \Omega_{\text{ROI}}$). Right: MAP estimate with the multiresolution model using $J_{\text{out}} = 1$ scaling levels outside the ROI while the number of scaling levels inside the ROI was $J = 6$.

(the number of unknown pixels $m = 248\,004$) is shown in the left image in figure 9 and the MAP estimate with total variation prior ($m = 248\,004$) is shown in the middle. On the right is the MAP estimate with the multiresolution model using only the coarsest scaling level ($J_{\text{out}} = 1$) outside the ROI while the number of scaling levels inside the ROI was $J = 6$ (the number of unknown wavelet coefficients $n = 29\,130$). The computation time for the MAP estimate with TV prior was 12 min 36 s and 2 min 14 s with the multiresolution model.

The left image in figure 10 shows the MAP estimate with the total variation prior when the truncated measurement model A_{ROI}, equation (26), is employed. In this case, the number of unknown pixels is $m = 19\,044$. The right image shows the MAP estimate with the

multiresolution model when only the coarsest scaling level $J_{\text{out}} = 1$ is used outside the ROI. As can be seen, the reconstruction with the truncated model has again severe artifacts near the boundary $\partial\Omega_{\text{ROI}}$ and is inferior to the reconstruction with the multiresolution model.

The results in figures 8–10 have a very similar trend compared to those in section 6.1 with simulated local tomography data; the results suggest that the multiresolution model can be used for high quality reconstruction of the ROI with significantly smaller number of unknowns compared to the conventional pixel-based models. Note also that the computation time with the multiresolution model was clearly shorter than with the TV model in the comparison in figure 9.

7. Conclusions

We propose a Bayesian multiresolution model for local tomography in dental radiology. The model uses a Besov norm prior and a wavelet representation of the tissue structures. All the available scaling levels of the wavelets are used inside the region of interest (ROI), and a smaller number of scaling levels outside the ROI. A gradient-based optimization algorithm is implemented for the computation of the MAP estimate, which is then displayed as the reconstruction. The feasibility of our model is evaluated using simulated and *in vitro* data in local tomography settings. Our model allows high quality reconstruction of the ROI in a computationally efficient form; the model produces similar image quality in the ROI than the current state-of-the-art pixel-based methods while significantly reducing degrees of freedom. In the test case with real data the computation time is reduced to less than 20%.

Here the method is evaluated with 2D examples. The significance of the dimensionality reduction is expected to be even more important in the 3D case where the ratio of the ROI volume to the whole image volume is typically smaller than in 2D. Thus our model is a promising platform for 3D local tomography reconstruction in dental cone beam computed tomography.

Acknowledgments

The authors would like to thank the National Technology Agency of Finland (TEKES) and the Academy of Finland (projects 108299, 119270 and Finnish Programme for Centres of Excellence in Research 2006-2011, application number 213476) for the financial support of this work. We would also like to thank the PaloDEx Group for their participation and support.

References

Aboufadel E and Schlicker S 1999 *Discovering Wavelets* (Canada: Wiley)

Antyufeev V S and Bondarenko A N 1996 X-ray tomography in scattering media *SIAM J. Appl. Math.* **56** 573–87

Bhatia M, Karl W C and Willsky A S 1996 A wavelet-based method for multiscale tomographic reconstruction *IEEE Trans Med. Imag.* **15** 92–101

Bonnet S, Peyrin F, Turjman F and Prost R 2000 Tomographic reconstruction using nonseparable wavelets *IEEE Trans. Image Process.* **9** 1445–50

Bouman C and Sauer K 1993 A generalized Gaussian image model for edge-preserving MAP estimation *IEEE Trans. Image Process.* **2** 296–310

Candes E, Romberg J and Tao T 2006 Robust uncertainty principles: Exact signal reconstruction from highly incomplete frequency information *IEEE Trans. Inf. Theory* **52** 489–509

Chambolle A, DeVore R A, Lee N and Lucier B J 1998 Nonlinear wavelet image processing: variational problems, compression, and noise removal through wavelet shrinkage *IEEE Trans. Image Process.* **7** 319–35

Choi H and Baraniuk R G 2004 Multiple wavelet basis image denoising using Besov ball projections *IEEE Signal Process. Lett.* **11** 717–20

Dai Y H and Yuan Y 1999 A nonlinear conjugate gradient method with a strong global convergence property *SIAM J. Optim.* **10** 177–82

Daubechies I 1992 *Ten Lectures on Wavelets* (Philadelphia, PA: SIAM)

Delaney A H and Bresler Y 1995 Multiresolution tomographic reconstruction using wavelets *IEEE Trans. Image Process.* **4** 799–813

Delaney A H and Bresler Y 1998 Globally convergent edge-preserving regularized reconstruction: an application to limited-angle tomography *IEEE Trans. Image Process.* **7** 204–21

Dobson D C and Santosa F 1994 An image enhancement technique for electrical impedance tomography *Inverse Problems* **10** 317–34

Dobson D C and Santosa F 1996 Recovery of blocky images from noisy and blurred data *SIAM J. Appl. Math.* **56** 1181–98

Dobson D C and Vogel C R 1997 Convergence of an iterative method for total variation denoising *SIAM J. Numer. Anal.* **34** 1779–91

Ekestubbe A, Gröndahl K and Gröndahl H-G 1997 The use of tomography for dental implant planning *Dentomaxillofac. Radiol.* **26** 206–13

Faridani A, Finch D V, Ritman E L and Smith K T 1997 Local tomography: II *SIAM J. Appl. Math.* **57** 1095–127

Faridani A, Ritman E L and Smith K T 1992 Local tomography *SIAM J. Appl. Math.* **52** 459–84

Frese T, Bouman C and Sauer K 2002 Adaptive wavelet graph model for Bayesian tomographic reconstruction *IEEE Trans. Image Process.* **7** 756–70

Hanson K M 1987 Bayesian and related methods in image reconstruction from incomplete data *Image Recovery: Theory and Application* (Orlando, FL: Academic) pp 79–125

Hanson K M and Wecksung G W 1983 Bayesian approach to limited angle reconstruction in computed tomography *J. Opt. Soc. Am.* **73** 1501–9

Hanson K M and Wecksung G W 1985 Local basis-function approach to computed tomography *Appl. Opt.* **24** 4028–39

Hitachi Medical Corp. (Japan) CB Mercuray Dentomaxillofacial Cone Beam CT-System. 2006 (online), available: http://www.hitachi-medical.co.jp/english/product/cbct/mercuray/index.html

Härdle W, Kerkyacharian G, Picard D and Tsybakov A 1998 *Wavelets, Approximation and Statistical Applications (Lecture Notes in Statistics)* (New York: Springer)

Imaging Sciences International (USA) i-CAT Cone Beam 3-D Dental Imaging System 2006 (online), available: http://www.imagingsciences.com/pro_iCAT.html

Jaffard S 2004 Beyond Besov spaces part 1: distributions of wavelet coefficients *J. Fourier Anal. Appl.* **10** 221–46

Kaipio J P, Kolehmainen V, Somersalo E and Vauhkonen M 2000 Statistical inversion and Monte Carlo sampling methods in electrical impedance tomography *Inverse Problems* **16** 1487–522

Kaipio J and Somersalo E 2005 *Statistical and Computational Inverse Problems* (New York: Springer)

Keinert F 2004 *Wavelets and Multiwavelets* (Boca Raton, FL: Chapman and Hall)

Kolehmainen V, Siltanen S, Järvenpää S, Kaipio J P, Koistinen P, Lassas M, Pirttilä J and Somersalo E 2003 Statistical inversion for medical x-ray tomography with few radiographs: II. Application to dental radiology *Phys. Med. Biol.* **48** 1465–90

Kolehmainen V, Vanne A, Siltanen S, Järvenpää S, Kaipio J P, Lassas M and Kalke M 2006 Parallelized Bayesian inversion for three-dimensional dental x-ray imaging *IEEE Trans. Med. Imaging* **25** 218–28

Lehtinen M S 1998 On statistical inversion theory *Theory and Applications of Inverse Problems* ed H Haario (London: Longman)

Lewitt R M 1992 Alternatives to voxels for image representation in iterative reconstruction algorithms *Phys. Med. Biol.* **37** 705–16

Maass P 1992 The interior Radon transform *SIAM J. Appl. Math.* **52** 710–24

Madych W R 1999 Tomography, approximate reconstruction and continuous wavelet transforms *Appl. Comput. Harmon. Anal.* **7** 54–100

Meyer Y 1992 *Wavelets and Operators* (Cambridge: Cambridge University Press)

Mosegaard K and Tarantola A 1995 Monte Carlo sampling of solutions to inverse problems *J. Geophys. Res.* B **14** 12431–47

Mueller K 1998 Fast and accurate three-dimensional reconstruction from cone-beam projection data using algebraic methods *PhD Dissertation* Ohio Sate University, Columbus, OH (online) available: http://www.cs.sunysb.edu/mueller/research/ct.html

Natterer F 1986 *The Mathematics of Computerized Tomography* (Philadelphia, PA: Wiley)

Nicholls G K and Fox C 1998 Prior modelling and posterior sampling in impedance imaging *Bayesian Inference for Inverse Problems (Proc. SPIE vol 3459)* ed A Mohammad-Djafari (Bellingham, WA: SPIE Optical Engineering Press) pp 116–27

Olson T and DeStefano J 1994 Wavelet localization of the Radon transform *IEEE Trans. Signal Process.* **42** 2055–67

Persson M, Bone D and Elmqvist H 2001 Total variation norm for three-dimensional iterative reconstruction in limited view angle tomography *Phys. Med. Biol.* **46** 853–66

Planmeca Incorp. (USA), ProMax 3D 2006 (online) available: http://www.planmeca.com/EN/dental_x-rays/planmeca_promax_3d/

Ramesh A, Ludlow J B, Webber R L, Tundall D A and Paquette D 2002 Evaluation of tuned-aperture computed tomography in the detection of simulated periodontal defects *Oral Maxillofac. Radiol.* **93** 341–9

Rantala M, Vänskä S, Järvenpää S, Kalke M, Lassas M, Moberg J and Siltanen S 2006 Wavelet-based reconstruction for limited-angle x-ray tomography *IEEE Trans. Med. Imaging* **25** 210–7

Rashid-Farrokhi F, Liu K J R, Berenstein C A and Walnut D 1997 Wavelet-based multiresolution local tomography *IEEE Trans. Image Process.* **6** 1412–30

Rudin L I, Osher S and Fatemi E 1992 Nonlinear total variation based noise removal algorithms *Physica* D **60** 259–68

Sahiner B and Yagle A E 1993 Limited angle tomography using wavelets *Nuclear Science Symp. IEEE Conf. Record* **3** 1912–16

Sauer K, James S Jr and Klifa K 1994 Bayesian estimation of 3-D objects from few radiographs *IEEE Trans. Nucl. Sci.* **41** 1780–90

Sidky E Y, Kao C-M and Pan X 2006 Effect of the data constraint on few-view, fan-beam CT image reconstruction by TV minimization *Nuclear Science Symp. IEEE Conf. Record* pp 2296–98

Siltanen S, Kolehmainen V, Järvenpää S, Kaipio J P, Koistinen J, Lassas M, Pirttilä J and Somersalo E 2003 Statistical inversion for medical x-ray tomography with few radiographs: I. Genereal theory *Phys. Med. Biol.* **48** 1437–63

Smith K T and Keinert F 1985 Mathematical foundations of computed tomography *Appl. Opt.* **24** 3950–7

Soredex (Finland), SCANORA® 3D, 2007 (online) available: http://www.soredex.com/pdf/SCANORA_3D_FINAL_LowRes.pdf

Steinberg B Z and Heyman E 1993 The local Radon transform and variable scale resolution with application to time-dependent wave radiation *SIAM J. Appl. Math.* **53** 381–400

Sukovic P and Clinthorne N H 2000 Penalized weighted least squares image reconstruction for dual energy x-ray transmission tomography *IEEE Trans. Med. Imaging* **19** 1075–81

Vassilevski P S and Wade J G 1997 A comparison of multilevel methods for total variation regularization *Electron. Trans. Numer. Anal.* **6** 255–70

Vidakovic B 1999 *Statistical Modeling by Wavelets (Wiley Series in Probability and Statistics)* (Canada: Wiley)

Zhao S, Welland G and Wang G E 1997 Wavelet sampling and localization schemes for the Radon transform in two dimensions *SIAM J. Appl. Math.* **57** 1749–63

Zheng J, Saquib S, Sauer K and Bouman C A 2000 Parallelizable Bayesian tomography algorithms with rapid guaranteed convergence *IEEE Trans. Image Process.* **9** 1745–59

Zhong J, Ning R and Conover D 2004 Image denoising based on multiscale singularity detection for cone beam CT breast imaging *IEEE Trans. Med. Imag.* **23** 696–703